

# High Capacity and Energy Density of Zn–Ni–Co–P Nanowire Arrays as an Advanced Electrode for Aqueous Asymmetric Supercapacitor

Xueyan Lei, Shicheng Ge, Yihong Tan, Zhi Wang, Jing Li, Xuefeng Li, Guojing Hu, Xingqun Zhu, Meng Huang, Yanwu Zhu, and Bin Xiang\*



Cite This: *ACS Appl. Mater. Interfaces* 2020, 12, 9158–9168



Read Online

ACCESS |



Metrics & More



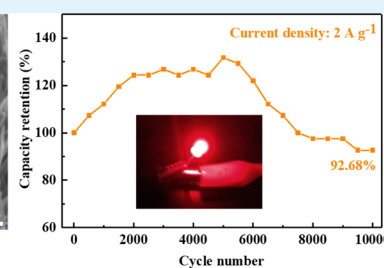
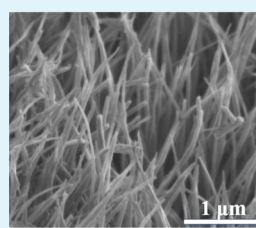
Article Recommendations



Supporting Information

**ABSTRACT:** Developing multicomponent transition-metal phosphides has become an efficient way to improve the capacitive performance of single-component transition-metal phosphides. However, reports on quaternary phosphides for supercapacitor applications are still scarce. Here, we report high capacity and energy density of Zn–Ni–Co–P quaternary phosphide nanowire arrays on nickel foam (ZNCP-NF) composed of highly conductive metal-rich phosphides as an advanced binder-free electrode in aqueous asymmetric supercapacitors. In a three-electrode system using the new electrode, a high specific capacity of  $1111 \text{ C g}^{-1}$  was obtained at a current density of  $10 \text{ A g}^{-1}$ . Analysis of this aqueous asymmetric supercapacitor with ZNCP-NF as the positive electrode and commercial activated carbon as the negative electrode reveals a high energy density ( $37.59 \text{ Wh kg}^{-1}$  at a power density of  $856.52 \text{ W kg}^{-1}$ ) and an outstanding cycling performance (capacity retention of 92.68% after 10 000 cycles at  $2 \text{ A g}^{-1}$ ). Our results open a path for a new design of advanced electrode material for supercapacitors.

**KEYWORDS:** quaternary phosphide, metal-rich phosphides, nanowire arrays, binder-free electrode, aqueous asymmetric supercapacitor



## 1. INTRODUCTION

Supercapacitors have attracted extensive attention in the development of high-performance energy storage devices around the world because of their ultrahigh power output, ultrafast charging and discharging rates, long cycling life, safety, and eco-friendliness.<sup>1–5</sup> However, supercapacitors are limited in practical applications due to their intrinsically lower energy density.<sup>6</sup> Obtaining higher operating voltage and specific capacity is the entry point to improving energy density. Although the operating voltage can be raised to beyond 2 V and even 3 V by using organic electrolytes, these organic electrolytes are poor ionic conductors and are especially expensive and toxic.<sup>6</sup> In contrast, the electrolytes of aqueous symmetric supercapacitors are not toxic. However, the operating voltage of aqueous symmetric supercapacitors is usually kept lower than 1.0 V to avoid the water-splitting reaction.<sup>6,7</sup> Therefore, an increasing amount of attention has been devoted to aqueous asymmetric supercapacitors (AASs), which can make full use of the different potential windows of the cathode and anode to offer a wider working voltage, and thereby distinctly enhance the energy density.<sup>8</sup>

Recently, transition-metal phosphides (TMPs) have attracted intense interest for applications in anodic materials of asymmetric supercapacitors because of their high conductivity, superior redox activity, metalloid characteristics, and good thermal and environmentally friendly properties.<sup>9–11</sup> However, due to the irreversibility of the faradic reaction, poor structural

stability, and electrochemical stability, the rate performance and cycling life of single-component TMPs still need to be improved compared to those of commercial supercapacitors.<sup>11–13</sup> Fortunately, compared to single-component TMPs, mixed TMPs by introduction of hetero-metal ions can be utilized to improve the rate performance, electrochemical capacitive performance, and electrochemical stability, for example, Ni–Co–P.<sup>14</sup> This improvement is due to the richer faradic reaction kinetics benefited from metallic characteristics of mixed TMPs and multiple oxidation states of different metals.<sup>12–15</sup> Research on quaternary phosphides has been focused on further improvement of the performance of TMPs in asymmetric supercapacitors because of the special structure and components of quaternary phosphides. For example, the nickel–cobalt–molybdenum phosphides on carbon cloth<sup>10</sup> have exhibited a specific capacitance as high as  $433 \text{ F g}^{-1}$  at a current density of  $1 \text{ A g}^{-1}$  and a long-term cycling stability characterized by 82.4% retention after 10 000 cycles. In addition, because Zn presents high chemical activity and good electrical conductivity, it has been reported that the electrochemical properties of materials can be improved by Zn

**Received:** September 28, 2019

**Accepted:** January 31, 2020

**Published:** January 31, 2020



doping.<sup>1,5,13</sup> For example, metal-organic framework (MOF)-derived NiZnCoP nanosheet arrays<sup>16</sup> on carbon nanotube fibers have displayed impressive electrochemical performance with a capacity of 0.092 mAh cm<sup>-2</sup> and energy density of 30.61 mWh cm<sup>-3</sup>.

It is worth noting that the P content in the phase composition of the TMPs greatly influences the conductivity since P atoms with more electronegativity cause electrons in TMPs to be localized around P atoms.<sup>17</sup> Too many P atoms in the phase composition of the TMPs can weaken their conductivity, but a proper metal content in the phase composition of TMPs can enhance their conductivity instead.<sup>18</sup> However, how to design a structure of quaternary TMPs with an effective composition remains challenging.

Herein, we report high capacity and energy density of Zn–Ni–Co–P quaternary phosphide nanowire arrays on nickel foam (ZNCP-NF) composed of metal-rich phosphides as a binder-free electrode for aqueous asymmetric supercapacitors. The morphology, structure, and chemical composition of ZNCP-NF were characterized by field emission scanning electron microscopy (FESEM), transmission electron microscopy (TEM), high-resolution TEM (HRTEM), scanning transmission electron microscopy (STEM), energy-dispersive X-ray spectrometry (EDS), N<sub>2</sub> adsorption/desorption isotherms experiment, elemental mapping, X-ray diffractometry (XRD), and X-ray photoelectron spectroscopy (XPS). Cyclic voltammetry (CV), electrochemical impedance spectroscopy (EIS), and galvanostatic charge/discharge (GCD) and cycling stability tests were carried out to investigate the electrochemical properties of ZNCP-NF utilized as the electrode material in our new aqueous asymmetric supercapacitors.

## 2. EXPERIMENTAL SECTION

**2.1. Chemicals and Reagents.** The chemicals with analytical grade purity, such as nickel nitrate hexahydrate [Ni(NO<sub>3</sub>)<sub>2</sub>·6H<sub>2</sub>O], zinc nitrate hexahydrate [Zn(NO<sub>3</sub>)<sub>2</sub>·6H<sub>2</sub>O], cobalt nitrate hexahydrate [Co(NO<sub>3</sub>)<sub>2</sub>·6H<sub>2</sub>O], ammonium fluoride (NH<sub>4</sub>F), urea [(NH<sub>2</sub>)<sub>2</sub>CO], sodium hypophosphite monohydrate (NaH<sub>2</sub>PO<sub>2</sub>·H<sub>2</sub>O), acetone (CH<sub>3</sub>COCH<sub>3</sub>), absolute ethyl alcohol (C<sub>2</sub>H<sub>5</sub>OH, 99.5%), and potassium hydroxide (KOH, ≥99%), were purchased from Sinopharm Chemical Reagent Co., Ltd. and used directly without any further treatment. The model number of commercial activated carbon (AC) is YP50F.

**2.2. Synthesis of Materials.** A few pieces of nickel foams (2 cm × 1 cm) were pretreated with acetone, deionized (DI) water, and ethanol in an ultrasonication bath each for 30 min to remove impurities from the foam surface. Zn–Ni–Co precursors were prepared in a mixed solution containing 3 mmol Zn(NO<sub>3</sub>)<sub>2</sub>·6H<sub>2</sub>O, 3 mmol Ni(NO<sub>3</sub>)<sub>2</sub>·6H<sub>2</sub>O, 6 mmol Co(NO<sub>3</sub>)<sub>2</sub>·6H<sub>2</sub>O, 4 mmol NH<sub>4</sub>F, 12 mmol urea, and 70 mL of deionized (DI) water. The mixture was stirred for 30 min and then transferred into a 100 mL Teflon-lined stainless steel autoclave. Before the cleaned nickel foams were immersed in the solution, the back of the nickel foams were protected with tape to avoid contamination with reactants. The reaction was carried out at 130 °C for 5 h and then cooled down to room temperature. The as-prepared Zn–Ni–Co precursors were immersed in DI water in an ultrasonication bath for 20 min to remove the loose reaction product and then carefully rinsed with DI water and ethanol. Then, the Zn–Ni–Co precursors were dried at 80 °C for 24 h in an oven and the amount of the Zn–Ni–Co precursors loaded on the substrate was 2.46 mg cm<sup>-2</sup> on average. ZNCP-NF was synthesized by an effective phosphorization treatment of Zn–Ni–Co precursors with NaH<sub>2</sub>PO<sub>2</sub>·H<sub>2</sub>O. In detail, the Zn–Ni–Co precursor was loaded into a quartz boat and NaH<sub>2</sub>PO<sub>2</sub>·H<sub>2</sub>O (mass ratio with the precursor, 1:5) was placed at the adjacent side of the upstream 3 cm away from the Zn–Ni–Co precursors. Then, the Zn–Ni–Co precursors were

heat-treated at 350 °C for 2 h with a heating rate of 2 °C min<sup>-1</sup> in an argon atmosphere. For comparison, ZNCO-NF was fabricated according to ref 1 by heat treatment of the as-obtained Zn–Ni–Co precursors at 300 °C for 2 h with a heating rate of 2 °C min<sup>-1</sup> in the air atmosphere. The amount of ZNCP-NF and ZNCO-NF loaded on the substrate was 2.50 and 2.41 mg cm<sup>-2</sup> on average, respectively. The change of mass loading after hydrothermal and phosphating treatments is 0.04 mg cm<sup>-2</sup>.

**2.3. Materials Characterization.** A field emission scanning electron microscope (FEI Apreo), energy-dispersed X-ray spectrometer (FEI Apreo), transmission electron microscope (Japan JEM-2100F), high-resolution transmission electron microscope (Japan JEM-2100F), scanning transmission electron microscope (Japan JEM-2100F), elemental mapping device (Japan JEM-2100F), X-ray diffractometer with Cu K $\alpha$  radiation (MXPAHF, Mac Science Co. Ltd., Japan), X-ray photoelectron spectrometer (ESCALab 250, Thermo-VG Scientific), and N<sub>2</sub> adsorption/desorption apparatus (American Micromeritics Instrument Corporation TriStar II 3020M) were used to characterize the obtained samples.

**2.4. Electrochemical Measurements.** All electrochemical measurements were carried out at room temperature. Cyclic voltammetry (CV) and electrochemical impedance spectroscopy (EIS) for both the three-electrode system and two-electrode system were tested on CHI 660E electrochemical workstation. Galvanostatic charge/discharge (GCD) measurement for the three-electrode system was conducted on a CHI 660E electrochemical workstation. All electrochemical tests were performed after activation by 50 cycles at a scan rate of 20 mV s<sup>-1</sup> using the CV test. GCD and cycling performance test for the two-electrode system were carried out by applying a LAND battery program control test system (CT2001A, LANHE Co. Ltd., Wuhan).

For three-electrode system tests, ZNCP-NF and ZNCO-NF were selected as the working electrode, respectively. Pt foil was used as the counter electrode and Ag/AgCl as the reference electrode, with 3 mol L<sup>-1</sup> KOH aqueous solutions as the electrolyte. The mass-specific capacity  $Q$  (C g<sup>-1</sup>) of the as-prepared samples for the three-electrode setup was calculated according to eq 1

$$Q = \frac{I\Delta t}{m} \quad (1)$$

where  $I$  is the discharge current (mA),  $\Delta t$  is the discharge time (s), and  $m$  is the mass of the active materials (mg).

The asymmetric two-electrode system was assembled by directly employing the ZNCP-NF electrode without binder as the positive electrode and commercial activated carbon (AC) as the negative electrode in 3 mol L<sup>-1</sup> KOH aqueous electrolyte. The preparation of the AC negative electrode was proceeded as follows: active material (80 wt %), acetylene black (15 wt %), and an aqueous emulsion of poly(tetrafluoroethylene) (5%) (5 wt %) were mixed with a moderate amount of absolute alcohol to form a homogeneous slurry under continuous grinding in a mortar. The as-prepared mixture was pressed by a tablet machine to form a thin sheet. Finally, the thin sheet was pressed onto the nickel foam and then dried in an oven at 80 °C for 24 h. Finally, the AC electrode was obtained. The amount of AC loaded on the substrate was 2.04 mg cm<sup>-2</sup> on average. The mass-specific capacitance  $C$  (F g<sup>-1</sup>) of the as-prepared AC electrode was calculated according to eq 2

$$C = \frac{I\Delta t}{m\Delta V_-} \quad (2)$$

The optimum mass ratio of ZNCP-NF to AC in the asymmetric two-electrode system was calculated according to eq 3

$$\frac{m_+}{m_-} = \frac{C_- \times \Delta V_-}{Q_+} \quad (3)$$

where  $C_-$  is the specific capacitance of the negative electrode (F g<sup>-1</sup>),  $Q_+$  is the specific capacity of the positive electrode (C g<sup>-1</sup>),  $m$  is the mass of the positive (+) and negative (–) electrodes (mg), and  $\Delta V_-$  is the potential range of the negative (–) electrodes (V).

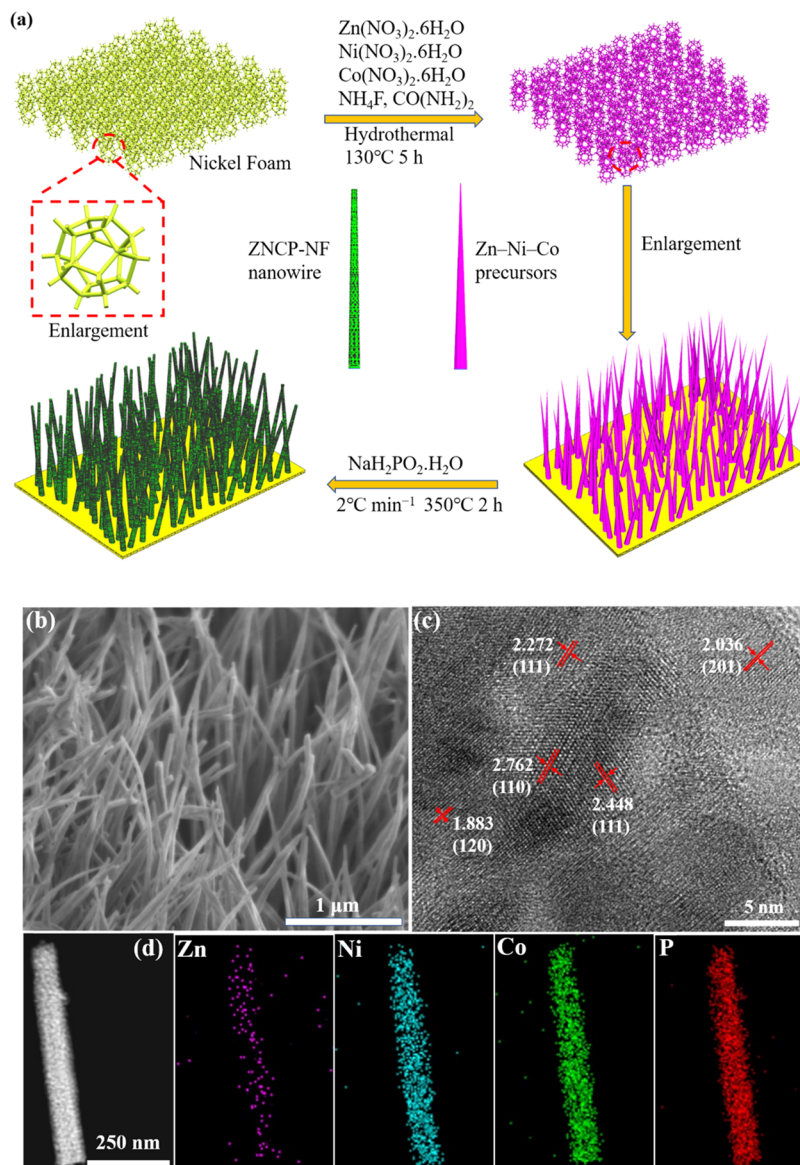


**Figure 1.** (a) Schematic illustration of the hierarchical ZNCP-NF materials synthesis strategy, (b) FESEM image, (c) HRTEM image, and (d) STEM image and the corresponding elemental mapping images of ZNCP-NF.

The mass-specific capacity  $Q$  ( $\text{C g}^{-1}$ ) and Coulombic efficiency  $\eta$  (%) of the as-prepared sample for the two-electrode setup were calculated from the GCD test according to eqs 4 and 5

$$Q = \frac{I \Delta t}{M} \quad (4)$$

$$\eta(\%) = \frac{\Delta t_1}{\Delta t_2} \quad (5)$$

where  $M$  is the total mass of the active materials on the positive and negative electrodes (mg),  $\Delta t_1$  is the discharge time (s), and  $\Delta t_2$  is the charge time (s). The energy density ( $E$ ,  $\text{Wh kg}^{-1}$ ) and power density ( $P$ ,  $\text{W kg}^{-1}$ ) were calculated via eqs 6 and 7, respectively

$$E = \frac{I \int V dt}{M \times 3.6} \quad (6)$$

$$P = \frac{E}{\Delta t} \times 3600 \quad (7)$$

where  $V$  is the operating potential of the discharge curve (V),  $dt$  is the time integration, and  $\Delta t$  is the discharge time (s).

### 3. RESULTS AND DISCUSSION

**3.1. Structure Characterizations.** The schematic process in Figure 1a demonstrates the synthesis of ZNCP-NF using nickel foam as the skeleton through a hydrothermal process followed by a phosphorization treatment process. The FESEM images of the precursors (Figure S1a,b, Supporting Information) present a morphology of one-dimensional (1D) uniform nanowire arrays grown densely on the surface of three-dimensional (3D) NF. After the phosphorization treatment, the morphology of ZNCP-NF (Figure 1b) remains uniform and hierarchical nanowire arrays, just as appeared in the precursor. Due to gas release and the erosion by  $\text{PH}_3$  during the phosphorization process, the nanowire surface becomes slightly rough, which implies more active sites have formed on the surface. HRTEM analysis was utilized to investigate the detailed structure of the as-prepared ZNCP-NF. The lattice fringes with lattice spacings of 1.883, 2.762, 2.448, 2.036, and 2.272 Å are shown in Figure 1c, corresponding to the (120), (110), (111), (201), and (111) lattice planes. The EDS

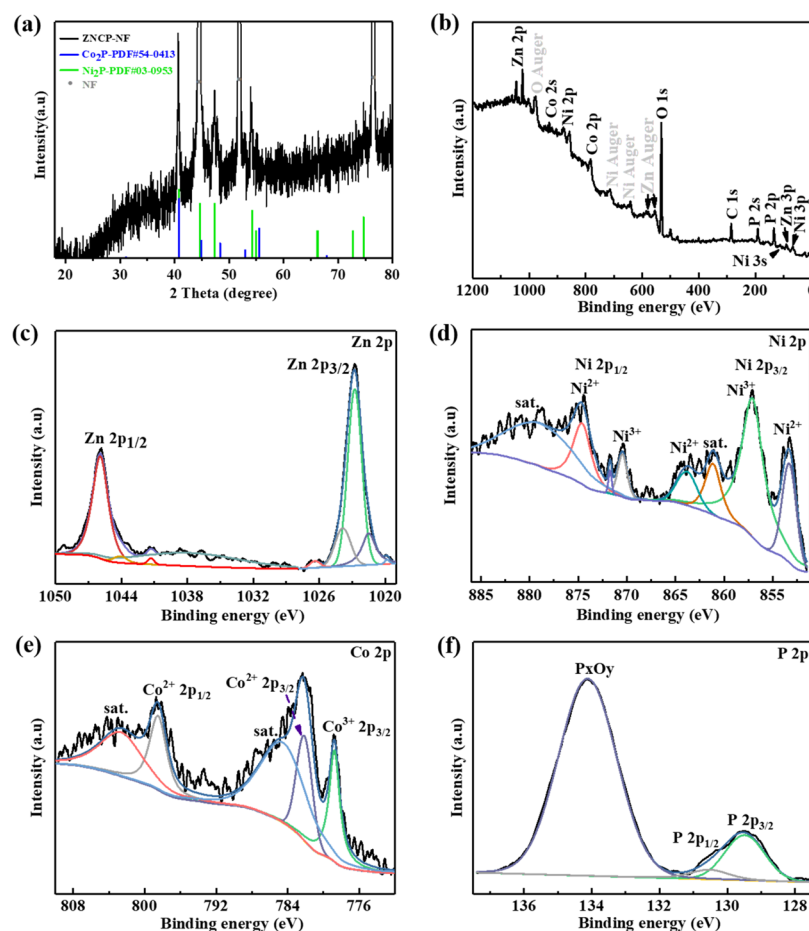


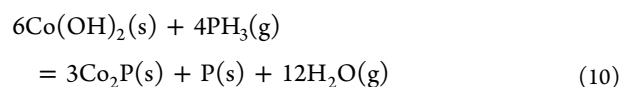
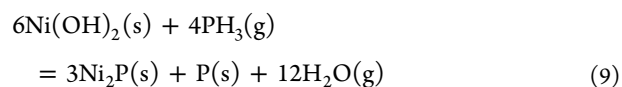
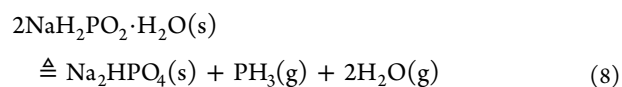
**Figure 2.** (a) XRD pattern, (b) XPS survey pattern, (c) high-resolution Zn 2p spectrum, (d) high-resolution Ni 2p spectrum, (e) high-resolution Co 2p spectrum, and (f) high-resolution P 2p spectrum of ZNCP-NF.

(Figure S2a, Supporting Information), STEM, and corresponding elemental mapping results (Figure 1d) reveal the ZNCP-NF elemental compositions with uniform distribution of Zn, Ni, Co, and P elements.

To gain insight into the specific surface area and porosity of the ZNCP-NF and ZNCO-NF material,  $N_2$  isothermal adsorption/desorption experiments were carried out (Figure S2b,c, Supporting Information). ZNCP-NF exhibits a large total pore volume and a large specific surface area of ZNCP-NF with a value of  $\sim 154.45 \text{ m}^2 \text{ g}^{-1}$  according to the Brunauer–Emmett–Teller (BET) model. The specific surface area of ZNCP-NF is higher than that of the ZNCO-NF and recent reports.<sup>19–21</sup> A typical type-IV curve and an H3-type hysteresis loop at  $P/P_0 = 0.45–1.0$  in Figure 2Sb (Supporting Information) indicate the presence of mesopore structures.<sup>22</sup> The inset in Figure 2Sb (Supporting Information) shows the pore size distribution of ZNCP-NF obtained by the Barrett–Joyner–Halenda (BJH) method, which reveals a typical mesoporous architecture with a suitable pore size distribution of 2.7–6 nm. The detailed specific surface area and porosity of the ZNCO-NF and ZNCP-NF are listed in Table S1 (Supporting Information).

XRD is a good tool to examine the crystalline phases of the as-synthesized materials. The XRD patterns of the Zn–Ni–Co precursors and the ZNCO-NF are depicted in Figure S2d (Supporting Information) and Figure S3 (Supporting Information), respectively. The diffraction peaks for ZNCP-NF (Figure 2a) can be well indexed to the representative peaks

of the  $\text{Co}_2\text{P}$  phase (JCPDS 54-0413),  $\text{Ni}_2\text{P}$  phase (JCPDS 03-0953), and Ni crystalline (JCPDS 65-2865). In detail, the peaks at  $40.6$ ,  $44.8$ ,  $48.4$ ,  $52.9$ , and  $55.4^\circ$  can be indexed to the (111), (021), (120), (002), and (030) planes of  $\text{Co}_2\text{P}$ , respectively.<sup>23</sup> The peaks at  $40.7$ ,  $44.5$ ,  $47.3$ ,  $54.1$ , and  $55.0^\circ$  can be indexed to the (111), (201), (210), (300), and (211) planes of  $\text{Ni}_2\text{P}$ , respectively.<sup>24</sup> In addition, three sharp diffraction peaks of the nickel foams could be clearly seen in the XRD pattern of ZNCP-NF, indicating the nickel foams were not involved in the reaction and still remained intact. The diffraction peaks corresponding to  $\text{Zn}_x\text{P}_y$  are not observed in the XRD pattern of ZNCP-NF, which may be ascribed to low content and poor crystallinity. With the above analysis, we can derive the chemical formulas for producing ZNCP-NF as follows<sup>19</sup>



The elemental compositions and the valence states of ZNCP-NF were analyzed by XPS as shown in Figure 2b–f. The XPS

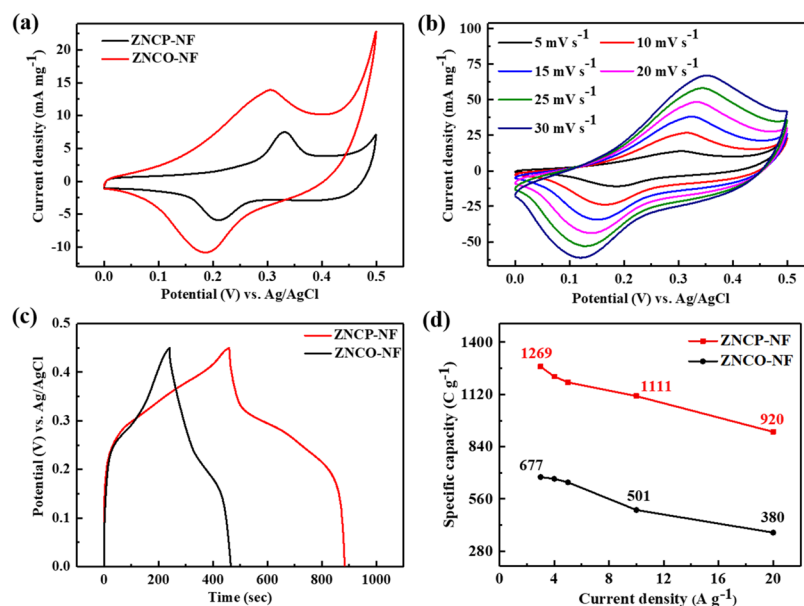
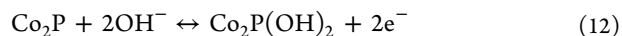
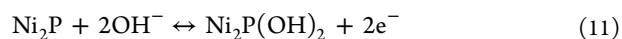


**Figure 3.** (a) CV curves of the ZNCP-NF and ZNCO-NF electrodes within an operating voltage range of 0–0.5 V at a scanning rate of 5 mV s<sup>-1</sup>. (b) CV curves within an operating voltage range of 0–0.5 V of the ZNCP-NF electrode at different scanning rates. (c) GCD curves of ZNCP-NF and ZNCO-NF within an operating voltage range of 0–0.45 V at a current density of 3 A g<sup>-1</sup>. (d) Specific capacity of the ZNCP-NF and ZNCO-NF electrodes at different current densities.

survey spectrum for ZNCP-NF (Figure 2b) indicates the existence of the elements Ni, Co, Zn, and P, consistent with the results of EDS and elemental mapping characteristics. The high-resolution Zn 2p spectrum (Figure 2c) shows two strong peaks at the binding energies of 1022.77 and 1045.92 eV, assigned to Zn 2p<sub>1/2</sub> and Zn 2p<sub>3/2</sub>, respectively.<sup>5</sup> The high-resolution Ni 2p<sub>3/2</sub> spectrum (Figure 2d) shows the main peaks at the binding energies of 853.29 eV (Ni<sup>2+</sup>), 857.07 eV (Ni<sup>3+</sup>), and 861.13 eV (the last is a shake-up satellite peak, identified as “sat.”). Also, the high-resolution Ni 2p<sub>1/2</sub> spectrum (Figure 2d) shows main peaks at the binding energies of 870.44 eV (Ni<sup>3+</sup>), 871.72 eV (Ni<sup>2+</sup>), and two shake-up satellite peaks at binding energies higher than those of the main peaks.<sup>13</sup> The high-resolution Co 2p spectrum (Figure 2e) has two peaks at 778.56 and 782.14 eV as well as a shake-up satellite peak at 784.5 eV corresponding to the spin-orbit splitting values of Co 2p<sub>3/2</sub>.<sup>25</sup> The peak at 798.5 eV and the shake-up satellite peak at 802.64 eV correspond to the spin-orbit splitting values of Co 2p<sub>1/2</sub>.<sup>25</sup> The binding energy at 778.56 eV for Co 2p<sub>3/2</sub> is the characteristic of Co<sup>3+</sup>.<sup>26</sup> The binding energies at 782.14 eV for Co 2p<sub>3/2</sub> and 798.5 eV for Co 2p<sub>1/2</sub> are the characteristic of Co<sup>2+</sup>.<sup>25</sup> The binding energies at 129.49 and 130.52 eV were indexed to P 2p<sub>3/2</sub> and P 2p<sub>1/2</sub>, respectively (Figure 2f).<sup>27</sup> The peak at 134.12 eV is assigned to phosphate species due to exposure to air.<sup>26</sup> The XPS analysis reveals that the atomic weight percentages of Zn, Co, Ni, and P in ZNCP-NF were 10.9, 15.35, 16.38, and 57.37 atom %, respectively.

**3.2. Electrochemical Performance Characterizations in Three-Electrode System.** The CV, GCD, and EIS tests were carried out to investigate the electrochemical properties of ZNCP-NF when it was used as the working electrode in the three-electrode system with a Ag/AgCl electrode as the reference electrode and a Pt foil as the counter electrode in 3 mol L<sup>-1</sup> KOH aqueous electrolyte, compared to the electrochemical performance of the ZNCO-NF, as shown in Figure 3. The CV curves of the ZNCP-NF and ZNCO-NF

electrodes within the voltage window of 0–0.5 V at a scanning rate of 5 mV s<sup>-1</sup> are shown in Figure 3a. A pair of nearly symmetrical redox peaks in the CV curve of ZNCP-NF indicated that favorable reversible redox reactions were observed.<sup>1</sup> The CV curve of ZNCP-NF displays a larger CV integral area and a higher peak current density of the redox reaction than the ZNCO-NF electrode, manifesting the better energy storage ability and ion diffusion.<sup>28</sup> The appearance of oxidation peaks at ~0.31 and ~0.18 V for ZNCP-NF electrodes can be attributed to the valence state changing from M<sup>2+</sup> to M<sup>3+</sup> (M = Co or Ni, Co<sup>2+</sup>/Co<sup>3+</sup>, and Ni<sup>2+</sup>/Ni<sup>3+</sup> transitions).<sup>11</sup> The related reaction mechanism can be described by the following chemical formulas<sup>19</sup>



When the scanning rates increase from 5 to 30 mV s<sup>-1</sup> (Figures 3b and S4a, Supporting Information), the response current density of the anodic and cathodic peaks increases, which may be related to the rapid redox reactions occurring at the active material/electrolyte interface.<sup>10</sup> And the positions of the anodic and cathodic peaks shift toward the positive and negative potentials, respectively, due to the polarization effect.<sup>20</sup> However, the shapes of the CV curves of ZNCP-NF (Figure 3b) are well maintained, indicating excellent rate capability.<sup>2</sup>

Figure 3c shows the GCD curves of ZNCP-NF and ZNCO-NF measured at the current density of 3 A g<sup>-1</sup> within the potential range of 0–0.45 V. The nonlinear and nearly symmetrical GCD curves with obvious charge/discharge plateaus further certify the behavior of redox reaction and the high Coulombic efficiency of ZNCP-NF.<sup>29,30</sup> According to eq 1, the longer the discharge time, the higher the specific capacity. Obviously, the discharge time of ZNCP-NF was much longer than that of the ZNCO-NF, indicating a higher specific capacity. The reason for this high specific capacity may

be the special composition and that the ordered nanofiber arrays grown on nickel foams facilitate the diffusion of electrolyte ions. This morphology may make electrolyte ions take more time to diffuse from the top end of nanowire arrays to the bottom.<sup>30</sup> Thus, the discharge time is longer.

The galvanostatic charge/discharge curves of ZNCP-NF and ZNCO-NF (Figure S4b,c, Supporting Information) were measured at different current densities of 3–20 A g<sup>-1</sup> within operating potential range of 0–0.45 V. In detail, the specific capacities of ZNCP-NF were calculated to be ~1269 C g<sup>-1</sup> (2820 F g<sup>-1</sup>), 1216 C g<sup>-1</sup> (2702 F g<sup>-1</sup>), 1185 C g<sup>-1</sup> (2633 F g<sup>-1</sup>), 1111 C g<sup>-1</sup> (2469 F g<sup>-1</sup>), and 920 C g<sup>-1</sup> (2044 F g<sup>-1</sup>), respectively, when the current densities were 3, 4, 5, 10, and 20 A g<sup>-1</sup>. The relationship between the specific capacity and current density of the ZNCP-NF electrode is shown in Figure 3d, which displays a high rate performance. The rate capability of ZNCP-NF is ~72.5% when the current densities increase from 3 to 20 A g<sup>-1</sup>, which is higher than that of the ZNCO-NF (56.1%). According to the above analysis, because of the special composition and structure of ZNCP-NF, the capacitive performance is far superior to those of the reported supercapacitors; the details are shown in Table S2 (Supporting Information).

Figure S4d shows the EIS curves of ZNCP-NF and ZNCO-NF acquired in the range of frequency of 10<sup>5</sup>–0.01 Hz under an open-circuit voltage of 1200 s (inset in Figure S4d is its corresponding high-frequency amplification), which consists of small circles in the high-frequency regions and a sloped line in the low-frequency regions. The intercept on the real axis represents the equivalent series resistance (*R*<sub>ESR</sub>), which is the sum of the ionic resistance of the electrolyte, the intrinsic resistance of the electrode material, and the interface resistance between the electrode active material and the substrate.<sup>22</sup> The diameter of small circles in the high-frequency regions reflects the charge transfer resistance (*R*<sub>ct</sub>). The linear plots in low frequency correspond to the Warburg impedance (*W*). To obtain the impedance parameters, Nyquist plots were fitted by Zview and the corresponding equivalent circuit is shown in Figure S5 (Supporting Information). The equivalent circuit impedance parameters are listed in Table S3 (Supporting Information). It shows the lower resistance of the ZNCP-NF electrode, which is the key factor allowing the higher specific capacity and better rate performance of ZNCP-NF than ZNCO-NF. In addition, the slope of ZNCP-NF is nearly vertical in the low-frequency region, unlike that of ZNCO-NF, indicating better ion diffusion behavior in ZNCP-NF than ZNCO-NF.<sup>6</sup>

To better understand the charge storage mechanism of ZNCP-NF, it is of importance to study the relationship between the response current (*i*) and the scanning rate (*v*) of CV curves using eqs 13 and 14<sup>31</sup>

$$i = i_{\text{cap}} + i_{\text{diff}} = av^b \quad (13)$$

$$\log i = \log a + b \log v \quad (14)$$

where *i*<sub>cap</sub> is the current related to the capacitive surface-controlled process (mA), *i*<sub>diff</sub> is the current related to the slow diffusion-controlled process (mA), *i* is the peak current (mA), *v* is the scanning rate (mV s<sup>-1</sup>) of CV measurements, and *a* and *b* are two adjustable parameters, respectively. The value of *b* can be obtained from the slope of the plots of log(*v*) versus log(*i*), which is generally used to identify material type and charge storage mechanism.<sup>32</sup> Two well-defined conditions can

be described as follows: (i) *b* = 0.5 represents the diffusion-controlled process and battery-type materials; (ii) *b* = 1 elucidates surface-controlled process and pseudocapacitive materials.<sup>31</sup> The larger the value of *b*, the greater the capacitive contribution.<sup>31</sup> For our as-prepared ZNCP-NF, the plot of log(*v*) versus log(*i*) of cathodic peak current (Figure S6a, Supporting Information) gives the *b* value of 0.96. The slope of log(*v*) versus log(*i*) of anodic peak current (Figure S6a, Supporting Information) is 0.88. Those *b* values indicate that the charge storage mechanism of ZNCP-NF is dominated by the capacitive surface-controlled process. The corresponding capacitive contribution can be analyzed by eq 15<sup>33</sup>

$$i(V) = i_{\text{cap}} + i_{\text{diff}} = k_1v + k_2v^{1/2} \quad (15)$$

where *i* and *V* are total current (mA) and specific potential (V) of CV curves, respectively, *k*<sub>1</sub>*v* represents the capacitive surface-controlled current (mA), and *k*<sub>2</sub>*v*<sup>1/2</sup> represents the diffusion-controlled current (mA). The total capacity consists of two contributions: diffusion-controlled and capacitive contributions. The corresponding percentage contributed was calculated (Figure S6b, Supporting Information), which manifests the capacitive contributions in ZNCP-NF of 77, 88, 92, 94, 95, and 97% at 5, 10, 15, 20, 25, and 30 mV s<sup>-1</sup>, respectively. As the scanning rate increases, the capacitive contribution increases and dominates the total contribution, which is consistent with the conclusion obtained from the value of *b*.

**3.3. Discussion.** As demonstrated above, the as-synthesized ZNCP-NF nanowire arrays as electrode material exhibit impressive electrochemical performance. The reasons why the ZNCP-NF material has such high performance are as follows. First, FESEM characterization reveals the 1D well-aligned and hierarchical nanowire structure of ZNCP-NF, which may help to improve the infiltration of the electrolyte, accelerate the transport and diffusion of the electrolyte ions/electrons, and shorten the charge transfer path.<sup>11,34</sup>

Second, TEM result reveals that the ZNCP-NF nanowire arrays are composed of nanoparticles with a rough surface, which may help to improve the infiltration rate of materials and add electrochemical active sites. Moreover, N<sub>2</sub> isothermal adsorption/desorption experiments prove the existence of a large specific surface area with suitable mesoporous distribution and large total pore volume structure in ZNCP-NF. This structure may provide a shorter distance and unhindered channel for electron transfer and ion diffusion during the electrochemical reaction, facilitating the electrochemical reactions.<sup>20</sup>

Third, XPS analysis demonstrates that the ZNCP-NF nanowire arrays contain multimetal ions (Zn<sup>2+</sup>, Ni<sup>2+</sup>, Ni<sup>3+</sup>, Co<sup>2+</sup>, and Co<sup>3+</sup>) and XRD confirms the ZNCP-NF nanowire arrays consist of two phases (Ni<sub>2</sub>P and Co<sub>2</sub>P), revealing that Zn<sup>2+</sup> may take the form of metal ions doping the ZNCP-NF material. The doping by Zn<sup>2+</sup> may not only facilitate high redox reaction kinetics because of its high chemical activity but also adjust the band gap to modify the electronic property of ZNCP-NF.<sup>13,15</sup> In addition, with the introduction of Zn<sup>2+</sup>, the Zn doping may cause certain lattice defects due to lattice mismatches that actuates P atoms with a strong electronegativity to attract more bonding electrons.<sup>6</sup> As a result, the electron-conduction channels for electrochemical reactions may be extensively enhanced by involving Zn<sup>2+</sup> to form the ZNCP-NF material.<sup>6</sup> In multimetal components, there may be

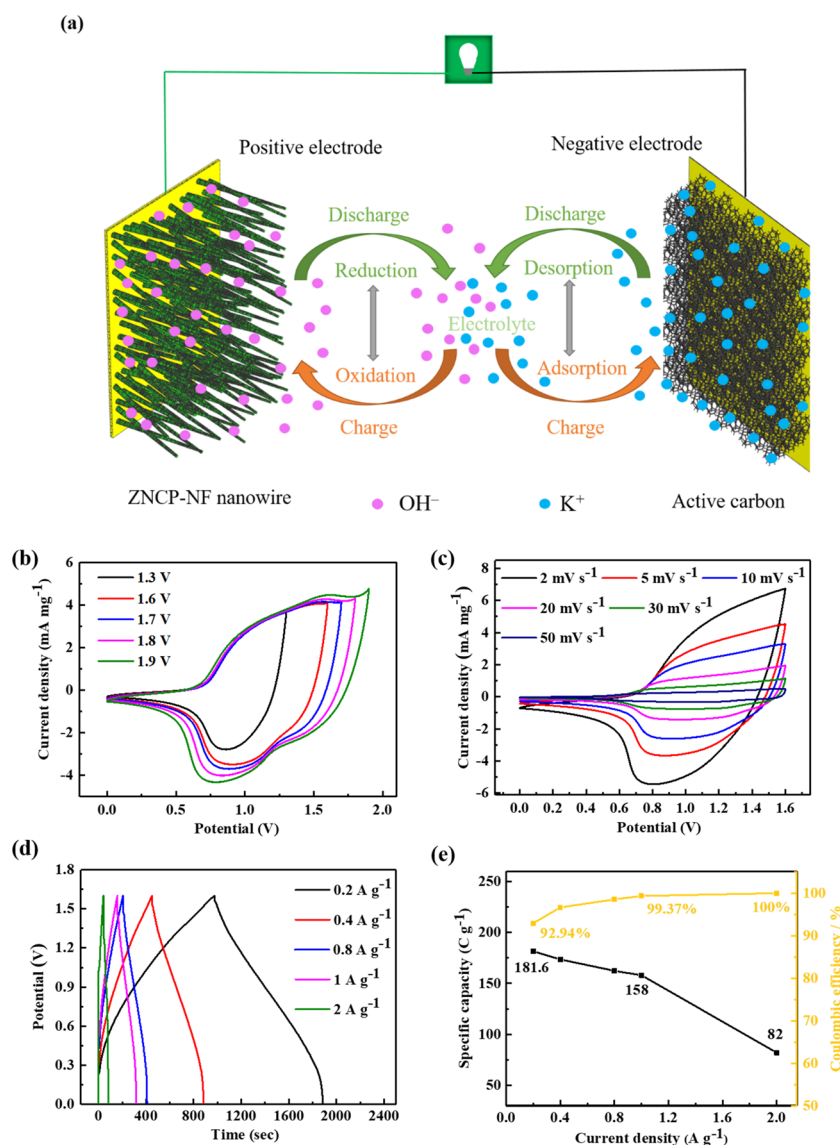


**Figure 4.** (a) Schematic illustration of the as-prepared asymmetric ZNCP-NF//AC supercapacitors. (b) CV curves of the ZNCP-NF//AC device within a different potential range of 1.3–1.9 V at a scanning rate of 30 mV s<sup>-1</sup>. (c) CV curves of the ZNCP-NF//AC device within an operating voltage range of 0–1.6 V at different scanning rates of 2–50 mV s<sup>-1</sup>. (d) GCD curves of the ZNCP-NF//AC device within an operating voltage range of 0–1.6 V at different current densities of 0.2–2 A g<sup>-1</sup>. (e) Specific capacity and Coulombic efficiency of the ZNCP-NF//AC device at different current densities.

a potential synergistic effect between the different metal ions. Due to the similarity of the d electron density of states between Ni–P/Co–P on one side and Pt on the other side, metal phosphides can behave in the same manner as noble metals, which means metal phosphide systems are highly attractive for catalysis.<sup>17</sup> These systems may mutually promote each other's Faraday reactions (Ni<sup>2+</sup>/Ni<sup>3+</sup> and Co<sup>2+</sup>/Co<sup>3+</sup>) with a low Gibbs free energy, thereby exhibiting stronger electrochemical activities, enhancing the reversibility of electrochemical reactions.

Fourth, the lower electronegativity of P atoms compared to O in transition metal oxides (TMOs) plays an important role to ensure fast electron transport and facilitate redox reactions, leading to better electrochemical performance than TMOs.<sup>11</sup> In addition, previous reports used density functional theory (DFT) calculations to verify that the P atoms at active sites in TMPs can achieve a nearly zero Gibbs free energy,<sup>35</sup> which may make the redox reaction more likely to occur.

Besides, TMPs can be classified into three types according to the atomic ratio of metal to phosphorus in chemical formula of TMPs (setting the ratio of metal to phosphorus as M/P =  $x$ ): (i)  $x > 1$ , metal-rich phosphides (e.g., M<sub>3</sub>P, M<sub>2</sub>P, MP), (ii)  $x = 1$ , monometal phosphides (e.g., MP), and (iii)  $x < 1$ , phosphorus-rich metal phosphides (e.g., MP<sub>2</sub>, MP<sub>3</sub>).<sup>18</sup> For phosphorus-rich metal phosphides, P atoms can greatly restrict the electron delocalization in TMPs since P atoms with more electronegativity compared to the lower electronegativity of metals could drag most of the valence electrons in metals.<sup>36</sup> The degree of electron delocalization promptly decreases along with the increase of P content, resulting in the TMPs gradually changing from having electrical conductivity to being a semiconductor and even an insulator.<sup>17</sup> This phenomenon explains why most phosphorus-rich metal phosphides are semiconductors and insulators with weak conductivity,<sup>17</sup> which usually weakens the electrochemical performance of supercapacitors. However, TMPs with an appropriate difference in

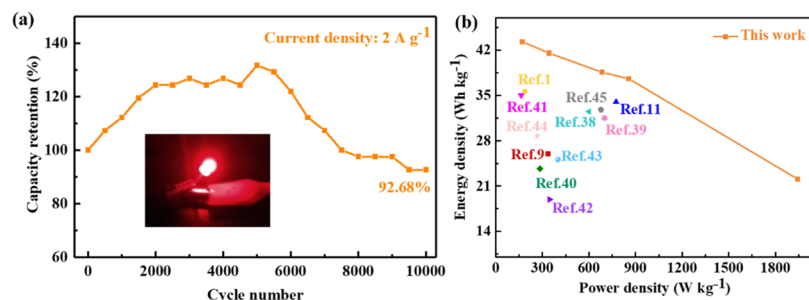


**Figure 5.** Cycle performance of the ZNCP//AC device at a current density of  $2 \text{ A g}^{-1}$  with 10 000 cycles; the inset shows a commercial red LED lighted by two ZNCP-NF//AC devices in series. (b) Ragone plots (energy density versus power density) of the ZNCP//AC device and reported asymmetric supercapacitors devices.

electronegativity between metal and phosphorus, and proper atomic ratio of metal to phosphorus, especially for the metal-rich phosphides, can exhibit a metalloid characteristic and highly conductive properties.<sup>17,18</sup> Therefore, we designed two phases of  $\text{Ni}_2\text{P}$  and  $\text{Co}_2\text{P}$  constituting our as-prepared ZNCP-NF materials, both of which are metal-rich phosphides with strong electrical conductivity, high thermal stability, and resistance to chemical attack.<sup>18</sup> In addition, ZNCP-NF was directly used as an electrode without any binder and polymer additive was directly grown on NF, which avoid “dead weight”, enlarge the ion-accessible surface, reduce contact resistance, shorten the efficient ion transport pathway, and strengthen the mechanical/chemical robustness of the electrode materials, thus improving the rate performance and cyclic stability.<sup>13</sup>

**3.4. Electrochemical Performance Characterizations in Two-Electrode System.** To further verify the practical application of ZNCP-NF, an aqueous asymmetric supercapacitor device (ZNCP-NF//AC) was assembled by using ZNCP-NF as the positive electrode and commercial activated carbon (AC) as the negative electrode in  $3 \text{ mol L}^{-1}$  KOH aqueous electrolyte. Detailed electrochemical characteristics of the AC electrode are presented in Figure S7a–d (Supporting Information). According to the CV curves at a scanning rate of  $5 \text{ mV s}^{-1}$  that the ZNCP-NF ( $0\text{--}0.5 \text{ V}$ ) and AC ( $0\text{ to }-1 \text{ V}$ ) electrodes obtained from the three-electrode system test (Figure S8a, Supporting Information), the overall capacity of the ZNCP-NF//AC device is derived from the combined contributions of the double-layer specific capacitance of the AC and the redox pseudocapacitance of ZNCP-NF.<sup>2</sup> To optimize the electrochemical performance of the ZNCP-NF//AC device, the optimized mass ratio of the AC and ZNCP-NF was calculated to be  $\sim 8.9$  by eq 3 according to the specific capacity obtained from the three-electrode system measurement at  $3 \text{ A g}^{-1}$ . The practical total loading mass of the active materials is  $\sim 25.5 \text{ mg}$ . A schematic illustration of the as-prepared asymmetric ZNCP-NF//AC supercapacitors is shown in Figure 4a. To choose a suitable potential window, the CV tests within various operating windows ranging from 1.3 to 1.9 V were carried out at a scanning rate of  $30 \text{ mV s}^{-1}$  (Figure 4b). When the voltage increases to 1.6 V, the shape of the CV curve remains almost constant without obvious polarization. Therefore, 1.6 V was selected as the potential window of ZNCP-NF//AC.

The CV, GCD, EIS, and cycling life tests were utilized to inspect the electrochemical properties of the ZNCP-NF//AC device. The CV curves at different scanning rates of  $2\text{--}50 \text{ mV s}^{-1}$  in ZNCP-NF//AC (Figure 4c) show similar shapes, indicating fast charge/discharge properties.<sup>1</sup> The GCD curves

at different current densities of  $0.2\text{--}2 \text{ A g}^{-1}$  in ZNCP-NF//AC (Figure 4d) exhibit nearly symmetrical triangular shapes, manifesting splendid capacitive performance and high rate performance.<sup>37</sup> The specific capacity was maintained at  $\sim 45.15\%$  of its initial capacity when the charge density increased to  $2 \text{ A g}^{-1}$  from  $0.2 \text{ A g}^{-1}$ . The EIS curve of the ZNCP-NF//AC device acquired at a frequency range of  $10^5\text{--}0.01 \text{ Hz}$  under an open-circuit voltage of 1200 s is shown in Figure S8b (Supporting Information). The plots of the specific capacity and Coulombic efficiency of the ZNCP-NF//AC device versus the different charge/discharge current densities (Figure 4e) confirm that the as-prepared device possesses a high Coulombic efficiency of  $\sim 100\%$  at a current density of  $2 \text{ A g}^{-1}$  and a high specific capacity ( $\sim 181.6 \text{ C g}^{-1}$  at the current density of  $0.2 \text{ A g}^{-1}$ ).

Cyclic stability is another evaluation criterion for the ZNCP-NF electrochemical performance. In the 10 000 cycles test at  $2 \text{ A g}^{-1}$  (Figure 5a), the specific capacity of the ZNCP-NF//AC device increases first, then decays slowly, and finally stabilizes. The reasons for specific capacity fluctuations could be as follows: the electrode soaking time and activation time in the electrolyte increase with the cycle number. Thus, the electrode material was gradually infiltrated from the surface into the interior and gradually activated, leading to the increase of effective electrochemical active sites.<sup>21,26,30</sup> In addition, repeated charging and discharging improve the electrolyte ion accessibility in the electrode material, leading to improved electrode utilization and enhanced effective contact area between the electrode material and electrolyte.<sup>9</sup> Therefore, the specific capacity gradually increases. After a period of cyclic charging and discharging, the electrolyte ions are repeatedly embedded and dislodged in the electrode material, resulting in the collapse and destruction of the electrode material morphology and structure. Therefore, the specific capacity is attenuated. When the electrode material is fully infiltrated and activated, with no obvious serious damage to the electrode morphology and structure, the specific capacity tends to be stable. After 10 000 cycles test at  $2 \text{ A g}^{-1}$ , the ZNCP-NF//AC device still showed high cyclic stability (capacity retention of 92.68%). The Ragone plot (energy density versus power density) of the ZNCP-NF//AC device compared to that of other previously reported transition-metal-based asymmetric supercapacitors devices is shown in Figure 5b. Our as-prepared asymmetric device exhibits an ultrahigh energy density of  $37.59 \text{ Wh kg}^{-1}$  at a power density of  $856.52 \text{ W kg}^{-1}$  and maintains an energy density of  $\sim 22.11 \text{ Wh kg}^{-1}$  at a high power density of  $\sim 1941.46 \text{ W kg}^{-1}$  at  $2 \text{ A g}^{-1}$ , which outclass the previously reported results (Figure 5b).<sup>1,9,11,38–45</sup> The inset in Figure 5a

shows that a commercial red light-emitting diode (LED) with a rated voltage of 2 V was lighted successfully by two ZNCP-NF//AC devices in series, verifying the feasibility of practical application. We attribute the remarkable electrochemical performance of the ZNCP-NF//AC device to the rational employment of the ZNCP-NF pseudocapacitive materials with high specific capacity as the positive electrode.

#### 4. CONCLUSIONS

In summary, we have successfully developed nickel foam-supported ZNCP-NF by a simple hydrothermal approach. The ZNCP-NF nanowire arrays deliver a high specific capacity of 1111 C g<sup>-1</sup> at 10 A g<sup>-1</sup> and a rate capability of 72.5% capacity retention when the current densities increase from 3 to 20 A g<sup>-1</sup> in the three-electrode system. ZNCP-NF//AC exhibits a high specific capacity of 181.6 C g<sup>-1</sup> at 0.2 A g<sup>-1</sup>, a high energy density of 37.59 Wh kg<sup>-1</sup> at a power density of 856.52 W kg<sup>-1</sup>, and an outstanding cyclic stability (capacity retention of 92.68% at 2 A g<sup>-1</sup> after 10 000 cycles). These excellent electrochemical behaviors demonstrate that the ZNCP-NF nanowire arrays are highly desirable for applications as supercapacitor electrode material.

#### ■ ASSOCIATED CONTENT

##### Supporting Information

The Supporting Information is available free of charge at <https://pubs.acs.org/doi/10.1021/acsami.9b17038>.

FESEM, TEM, and EDS spectra; XRD patterns; N<sub>2</sub> isothermal adsorption/desorption curves; electrochemical performance and so on (Figures S1–S15); BET result, comparison of capacity performance, and EIS (Tables S1–S3) (PDF)

#### ■ AUTHOR INFORMATION

##### Corresponding Author

**Bin Xiang** – Hefei National Research Center for Physical Sciences at the Microscale, Department of Materials Science & Engineering, CAS Key Laboratory of Materials for Energy Conversion, University of Science and Technology of China, 230026 Hefei, Anhui, China; Email: [binxiang@ustc.edu.cn](mailto:binxiang@ustc.edu.cn)

##### Authors

**Xueyan Lei** – Hefei National Research Center for Physical Sciences at the Microscale, Department of Materials Science & Engineering, CAS Key Laboratory of Materials for Energy Conversion, University of Science and Technology of China, 230026 Hefei, Anhui, China; [orcid.org/0000-0002-5483-7426](https://orcid.org/0000-0002-5483-7426)

**Shicheng Ge** – School of Mechanical Engineering, Nanjing University of Science and Technology, 210094 Nanjing, China

**Yihong Tan** – Department of Applied Chemistry, University of Science and Technology of China, 230026 Hefei, Anhui, China

**Zhi Wang** – Hefei National Research Center for Physical Sciences at the Microscale, Department of Materials Science & Engineering, CAS Key Laboratory of Materials for Energy Conversion, University of Science and Technology of China, 230026 Hefei, Anhui, China

**Jing Li** – Hefei National Research Center for Physical Sciences at the Microscale, Department of Materials Science & Engineering, CAS Key Laboratory of Materials for Energy Conversion, University of Science and Technology of China, 230026 Hefei, Anhui, China

**Xuefeng Li** – Hefei National Research Center for Physical Sciences at the Microscale, Department of Materials Science & Engineering, CAS Key Laboratory of Materials for Energy Conversion, University of Science and Technology of China, 230026 Hefei, Anhui, China

**Guojing Hu** – Hefei National Research Center for Physical Sciences at the Microscale, Department of Materials Science & Engineering, CAS Key Laboratory of Materials for Energy Conversion, University of Science and Technology of China, 230026 Hefei, Anhui, China

**Xingqun Zhu** – Hefei National Research Center for Physical Sciences at the Microscale, Department of Materials Science & Engineering, CAS Key Laboratory of Materials for Energy Conversion, University of Science and Technology of China, 230026 Hefei, Anhui, China; [orcid.org/0000-0003-1193-897X](https://orcid.org/0000-0003-1193-897X)

**Meng Huang** – Hefei National Research Center for Physical Sciences at the Microscale, Department of Materials Science & Engineering, CAS Key Laboratory of Materials for Energy Conversion, University of Science and Technology of China, 230026 Hefei, Anhui, China

**Yanwu Zhu** – Hefei National Research Center for Physical Sciences at the Microscale, Department of Materials Science & Engineering, CAS Key Laboratory of Materials for Energy Conversion, University of Science and Technology of China, 230026 Hefei, Anhui, China; [orcid.org/0000-0002-7505-1502](https://orcid.org/0000-0002-7505-1502)

Complete contact information is available at: <https://pubs.acs.org/doi/10.1021/acsami.9b17038>

#### Notes

The authors declare no competing financial interest.

#### ■ ACKNOWLEDGMENTS

This work was supported by the National Key Research and Development Program of China (2017YFA0402902) and the joint fund of the National Natural Science Foundation Committee of China Academy of Engineering Physics (NSAF) (U1630108). The authors also acknowledge the support of the USTC Center for Micro and Nanoscale Research and Fabrication.

#### ■ REFERENCES

- (1) Wu, C.; Cai, J.; Zhang, Q.; Zhou, X.; Zhu, Y.; Shen, P. K.; Zhang, K. Hierarchical Mesoporous Zinc-Nickel-Cobalt Ternary Oxide Nanowire Arrays on Nickel Foam as High-Performance Electrodes for Supercapacitors. *ACS Appl. Mater. Interfaces* **2015**, *7*, 26512–26521.
- (2) He, W.; Wang, C.; Li, H.; Deng, X.; Xu, X.; Zhai, T. Ultrathin and Porous Ni<sub>3</sub>S<sub>2</sub>/CoNi<sub>2</sub>S<sub>4</sub> 3D-Network Structure for Superhigh Energy Density Asymmetric Supercapacitors. *Adv. Energy Mater.* **2017**, *7*, No. 1700983.
- (3) Zhu, T.; Wang, J.; Ho, G. W. Self-supported yolk-shell nanocolloids towards high capacitance and excellent cycling performance. *Nano Energy* **2015**, *18*, 273–282.
- (4) Liu, Y.; Liu, G.; Nie, X.; Pan, A.; Liang, S.; Zhu, T. In situ formation of Ni<sub>3</sub>S<sub>2</sub>-Cu<sub>1.8</sub>S nanosheets to promote hybrid supercapacitor performance†. *J. Mater. Chem. A* **2019**, *7*, 11044–11052.
- (5) Li, C.; Balamurugan, J.; Kim, N. H.; Lee, J. H. Hierarchical Zn-Co-S Nanowires as Advanced Electrodes for All Solid State Asymmetric Supercapacitors. *Adv. Energy Mater.* **2018**, *8*, No. 1702014.

- (6) Choudhary, N.; Li, C.; Moore, J.; Nagaiah, N.; Zhai, L.; Jung, Y.; Thomas, J. Asymmetric Supercapacitor Electrodes and Devices. *Adv. Mater.* **2017**, *29*, No. 1605336.
- (7) Yu, M.; Lin, D.; Feng, H.; Zeng, Y.; Tong, Y.; Lu, X. Boosting the Energy Density of Carbon-Based Aqueous Supercapacitors by Optimizing the Surface Charge. *Angew. Chem.* **2017**, *129*, 5546–5551.
- (8) Sun, J.; Zhang, Q.; Wang, X.; Zhao, J.; Guo, J.; Zhou, Z.; Zhang, J.; Man, P.; Sun, J.; Li, Q.; Yao, Y. Constructing hierarchical dandelion-like molybdenum–nickel–cobalt ternary oxide nanowire arrays on carbon nanotube fiber for high-performance wearable fiber-shaped asymmetric supercapacitors. *J. Mater. Chem. A* **2017**, *5*, 21153.
- (9) Zhou, K.; Zhou, W.; Yang, L.; Lu, J.; Cheng, S.; Mai, W.; Tang, Z.; Li, L.; Chen, S. Ultrahigh-Performance Pseudocapacitor Electrodes Based on Transition Metal Phosphide Nanosheets Array via Phosphorization: A General and Effective Approach. *Adv. Funct. Mater.* **2015**, *25*, 7530–7538.
- (10) Yang, Y.; Zhou, Y.; Hu, Z.; Wang, W.; Zhang, X.; Qiang, L.; Wang, Q. 3D thin-wall cell structure nickel-cobalt-molybdenum ternary phosphides on carbon cloth as high-performance electrodes for asymmetric supercapacitors. *J. Alloys Compd.* **2019**, *772*, 683–692.
- (11) Li, X.; Wu, H.; Elshahawy, A. M.; Wang, L.; Pennycook, S. J.; Guan, C.; Wang, J. Cactus-Like NiCoP-NiCo-OH 3D Architecture with Tunable Composition for High-Performance Electrochemical Capacitors. *Adv. Funct. Mater.* **2018**, *28*, No. 1800036.
- (12) Liang, H.; Xia, C.; Jiang, Q.; Gandhi, A. N.; Schwingenschlög, U.; Alshareef, H. N. Low temperature synthesis of ternary metal phosphides using plasma for asymmetric supercapacitors. *Nano Energy* **2017**, *35*, 331–340.
- (13) Nguyen, T. T.; Balamurugan, J.; Kim, N. H.; Lee, J. H. Hierarchical 3D Zn-Ni-P Nanosheet Arrays as an Advanced Electrode for High-Performance All-Solid-State Asymmetric Supercapacitors. *J. Mater. Chem. A* **2018**, *6*, 8669.
- (14) Xu, W.; Wang, T.; Wang, H.; Zhu, S.; Liang, Y.; Cui, Z.; Yang, X.; Inoue, A. Free-standing amorphous nanoporous nickel cobalt phosphide prepared by electrochemically delloying process as a high performance energy storage electrode material. *Energy Storage Mater.* **2019**, *17*, 300–308.
- (15) Huang, J.; Wei, J.; Xiao, Y.; Xu, Y.; Xiao, Y.; Wang, Y.; Tan, L.; Yuan, K.; Chen, Y. Low temperature synthesis of ternary metal phosphides using plasma for asymmetric supercapacitors. *ACS Nano* **2018**, *12*, 3030–3041.
- (16) Zhang, Q.; Zhou, Z.; Pan, Z.; Sun, J.; He, B.; Li, Q.; Zhang, T.; Zhao, J.; Tang, L.; Zhang, Z.; Wei, L.; Yao, Y. All-Metal-Organic Framework-Derived Battery Materials on Carbon Nanotube Fibers for Wearable Energy-Storage Device. *Adv. Sci.* **2018**, *5*, No. 1801462.
- (17) Carenco, S.; Portehault, D.; Boissiere, C.; Mezailles, N.; Sanchez, C. Nanoscaled Metal Borides and Phosphides: Recent Developments and Perspectives. *Chem. Rev.* **2013**, *113*, 7981–8065.
- (18) Tian, S.; Li, X.; Wang, A.; Prins, R.; Chen, Y.; Hu, Y. Facile Preparation of Ni<sub>2</sub>P with a Sulfur-Containing Surface Layer by Low-Temperature Reduction of Ni<sub>2</sub>P<sub>2</sub>S<sub>6</sub>. *Angew. Chem., Int. Ed.* **2016**, *55*, 4030–4034.
- (19) Hou, S.; Xu, X.; Wang, M.; Xu, Y.; Lu, T.; Yao, Y.; Pan, L. Carbon-incorporated Janus-type Ni<sub>2</sub>P/Ni hollow spheres for high performance hybrid supercapacitors. *J. Mater. Chem. A* **2017**, *5*, 19054–19061.
- (20) Liang, M.; Zhao, M.; Wang, H.; Shen, J.; Song, X. Enhanced cycling stability of hierarchical NiCo<sub>2</sub>S<sub>4</sub>@Ni(OH)<sub>2</sub>@PPy core-shell nanotube arrays for aqueous asymmetric supercapacitors. *J. Mater. Chem. A* **2018**, *6*, 2482–2493.
- (21) Zhang, Q.; Zhao, B.; Wang, J.; Qu, C.; Sun, H.; Zhang, K.; Liu, M. High-performance hybrid supercapacitors based on self-supported 3D ultrathin porous quaternary Zn-Ni-Al-Co oxide nanosheets. *Nano Energy* **2016**, *28*, 475–485.
- (22) Gao, P.; Metz, P.; Hey, T.; Gong, Y.; Liu, D.; Edwards, D. D.; Howe, J. Y.; Huang, R.; Mixture, S. T. The critical role of point defects in improving the specific capacitance of d-MnO<sub>2</sub> nanosheets. *Nat. Commun.* **2017**, *8*, No. 14559.
- (23) Zhou, D.; Fan, L.-Z. Co<sub>2</sub>P nanoparticles encapsulated in 3D porous Ndoped carbon nanosheet networks as an anode for high-performance sodium-ion batteries†. *J. Mater. Chem. A* **2018**, *6*, 2139–2147.
- (24) Feng, Y.; Xu, C.; Hu, E.; Xia, B.; Ning, J.; Zheng, C.; Zhong, Y.; Zhang, Z.; Hu, Y. Construction of Hierarchical FeP@Ni<sub>2</sub>P Hollow Nanospindles for Efficient Oxygen Evolution. *J. Mater. Chem. A* **2018**, *6*, 14103–14111.
- (25) Jin, R.; Li, X.; Sun, Y.; Shan, H.; Fan, L.; Li, D.; Sun, X. Metal-Organic Frameworks-Derived Co<sub>2</sub>P@N-C@rGO with Dual Protection Layers for Improved Sodium Storage. *ACS Appl. Mater. Interfaces* **2018**, *10*, 14641–14648.
- (26) Elshahawy, A. M.; Guan, C.; Li, X.; Zhang, H.; Hu, Y.; Wu, H.; Pennycook, S. J.; Wang, J. Sulfur-doped cobalt phosphide nanotube arrays for highly stable hybrid supercapacitor. *Nano Energy* **2017**, *39*, 162–171.
- (27) Liu, T.; Li, A.; Wang, C.; Zhou, W.; Liu, S.; Guo, L. Interfacial Electron Transfer of Ni<sub>2</sub>P–NiP<sub>2</sub> Polymorphs Inducing Enhanced Electrochemical Properties. *Adv. Mater.* **2018**, *30*, No. 1803590.
- (28) Wu, X.; Xu, Y.; Hu, Y.; Wu, G.; Cheng, H.; Yu, Q.; Zhang, K.; Chen, W.; Chen, S. Microfluidic-spinning construction of black-phosphorus-hybrid microfibres for non-woven fabrics toward a high energy density flexible supercapacitor. *Nat. Commun.* **2018**, *9*, No. 4573.
- (29) Zhao, J.; Li, Z.; Yuan, X.; Yang, Z.; Zhang, M.; Meng, A.; Li, Q. A High-Energy Density Asymmetric Supercapacitor Based on Fe<sub>2</sub>O<sub>3</sub> Nanoneedle Arrays and NiCo<sub>2</sub>O<sub>4</sub>/Ni(OH)<sub>2</sub> Hybrid Nanosheet Arrays Grown on SiC Nanowire Networks as Free-Standing Advanced Electrodes. *Adv. Energy Mater.* **2018**, *8*, No. 1702787.
- (30) Tao, K.; Gong, Y.; Lin, J. Epitaxial grown self-supporting NiSe/Ni<sub>3</sub>S<sub>2</sub>/Ni<sub>12</sub>P<sub>5</sub> vertical nanofiber arrays on Ni foam for high performance supercapacitor: matched exposed facets and redistribution of electron density. *Nano Energy* **2019**, *55*, 65–81.
- (31) Liu, J.; Wang, J.; Xu, C.; Jiang, H.; Li, C.; Zhang, L.; Lin, J.; Shen, Z. X. Advanced Energy Storage Devices: Basic Principles, Analytical Methods, and Rational Materials Design. *Adv. Sci.* **2018**, *5*, No. 1700322.
- (32) Wang, X.; Mathis, T. S.; Li, K.; Lin, Z.; Vlcek, L.; Torita, T.; Osti, N. C.; Hatter, C.; Urbankowski, P.; Sarycheva, A.; Tyagi, M.; Mamontov, E.; Simon, P.; Gogotsi, Y. Influences from solvents on charge storage in titanium carbide MXenes. *Nat. Energy* **2019**, *4*, 241–248.
- (33) Liu, C.; Fu, H.; Pei, Y.; Wu, J.; Pisharodi, V.; Hu, Y.; Gao, G.; Yang, R. J.; Yang, J.; Cao, G. Understanding the electrochemical potential and diffusivity of MnO/C nanocomposites at various charge/discharge states†. *J. Mater. Chem. A* **2019**, *7*, 7831–7842.
- (34) Jin, T.; Han, Q.; Wang, Y.; Jiao, L. 1D Nanomaterials: Design, Synthesis, and Applications in Sodium–Ion Batteries. *Small* **2018**, *14*, No. 1703086.
- (35) Xiao, P.; Sk, M. A.; Thia, L.; Ge, X.; Lim, R. J.; Wang, J.-Y.; Lima, K. H.; Wang, X. Molybdenum phosphide as an efficient electrocatalyst for the hydrogen evolution reaction†. *Energy Environ. Sci.* **2014**, *7*, 2624–2629.
- (36) Shi, Y.; Zhang, B. Recent advances in transition metal phosphide nanomaterials: synthesis and applications in hydrogen evolution reaction. *Chem. Soc. Rev.* **2016**, *45*, 1529.
- (37) Li, H.; Lv, T.; Sun, H.; Qian, G.; Li, N.; Yao, Y.; Chen, T. Ultrastretchable and superior healable supercapacitors based on a double cross-linked hydrogel electrolyte. *Nat. Commun.* **2019**, *10*, No. 536.
- (38) Li, B.; Gu, P.; Feng, Y.; Zhang, G.; Huang, K.; Xue, H.; Pang, H. Ultrathin Nickel–Cobalt Phosphate 2D Nanosheets for Electrochemical Energy Storage under Aqueous/Solid-State Electrolyte. *Adv. Funct. Mater.* **2017**, *27*, No. 1605784.
- (39) Xu, Y.; Hou, S.; Yang, G.; Wang, X.; Lu, T.; Pan, L. Synthesis of bimetallic Ni<sub>x</sub>Co<sub>1-x</sub>P hollow nanocages from metalorganic frameworks for high performance hybrid supercapacitors. *Electrochim. Acta* **2018**, *285*, 192–201.

(40) Wang, X.; Sumboja, A.; Lin, M.; Yan, J.; Lee, P. S. Enhancing electrochemical reaction sites in nickel–cobalt layered double hydroxides on zinc tin oxide nanowires: a hybrid material for an asymmetric supercapacitor device. *Nanoscale* **2012**, *4*, 7266.

(41) Xu, K.; Li, W.; Liu, Q.; Li, B.; Liu, X.; An, L.; Chen, Z.; Zou, R.; Hu, J. Hierarchical mesoporous NiCo<sub>2</sub>O<sub>4</sub>@MnO<sub>2</sub> core–shell nanowire arrays on nickel foam for aqueous asymmetric supercapacitors†. *J. Mater. Chem. A* **2014**, *2*, 4795–4802.

(42) Ferreira, C. S.; Passos, R. R.; Pocrifka, L. A. Synthesis and properties of ternary mixture of nickel/cobalt/tin oxides for supercapacitors. *J. Power Sources* **2014**, *271*, 104–107.

(43) Suresh Babu, R.; Vinodh, R.; de Barros, A. L. F.; Samyn, L. M.; Prasanna, K.; Maier, M. A.; Alves, C. H. F.; Kim, H.-J. Asymmetric supercapacitor based on carbon nanofibers as the anode and two-dimensional copper cobalt oxide nanosheets as the cathode. *Chem. Eng. J.* **2019**, *366*, 390–403.

(44) Zhang, Z.; Zhang, H.; Zhang, X.; Yu, D.; Ji, Y.; Sun, Q.; Wang, Y.; Liu, X. Facile synthesis of hierarchical CoMoO<sub>4</sub>@NiMoO<sub>4</sub> core–shell nanosheet arrays on nickel foam as an advanced electrode for asymmetric supercapacitors. *J. Mater. Chem. A* **2016**, *4*, 18578–18584.

(45) Nagaraju, G.; Cha, S. M.; Sekhar, S. C.; Yu, J. S. Metallic Layered Polyester Fabric Enabled Nickel Selenide Nanostructures as Highly Conductive and Binderless Electrode with Superior Energy Storage Performance. *Adv. Energy Mater.* **2017**, *7*, No. 1601362.